Synchronous Reluctance Machines with and without Ferrite Assistance for Lifting Systems

Original
Synchronous Reluctance Machines with and without Ferrite Assistance for Lifting Systems / Ragazzo, P., Ferrari, S., Dilevrano, G., Beatrici, L., Girardi, C., Pellegrino, G.. - (2023), pp. 1-7. (2023 IEEE International Electric Machines & Drives Conference (IEMDC) San Francisco (CA) 15-18 May 2023) [10.1109/IEMDC55163.2023.10239091].

Availability:
This version is available at: 11583/2981878 since: 2023-09-10T19:21:25Z

Publisher:
ieee

Published
DOI:10.1109/IEMDC55163.2023.10239091

(Article begins on next page)

Synchronous Reluctance Machines with and without Ferrite Assistance for Lifting Systems

Paolo Ragazzo
Dipartimento Energia Galileo Ferraris
Politecnico di Torino
Turin, Italy
paolo.ragazzo@polito.it

Simone Ferrari
Dipartimento Energia Galileo Ferraris
Politecnico di Torino
Turin, Italy
simone.ferrari@polito.it

Gaetano Dilevrano
Dipartimento Energia Galileo Ferraris
Politecnico di Torino
Turin, Italy
gaetano.dilevrano@polito.it

Lorenzo Beatrici
ITG Tecnologie S.r.l.
Rovereto, Italy
lorenzobeatrici@itgtecnologie.it

Christian Girardi
ITG Tecnologie S.r.l.
Rovereto, Italy
christiangirardi@itgtecnologie.it

Gianmario Pellegrino
Dipartimento Energia Galileo Ferraris
Politecnico di Torino
Turin, Italy
gianmario.pellegrino@polito.it

***Abstract*—This paper deals with the comparative design and testing of synchronous reluctance machines with and without the addition of ferrite magnets for lifting applications. First, an efficient design process is proposed and showcased for both machine types. Given the application specifications of peak torque and maximum speed, the process permits quickly determining the cross-section of the motors, as well as the corresponding inverter current rating. Once the final design is defined, the optimal step-skewing angle is defined and applied in seamless computational time; for the ferrite-assisted machine, the demagnetization limit is assessed. After comparing the two designs in terms of key performance indexes and expected cost of production, the synchronous reluctance machine prototype was built and tested. The experimental tests include the measurement of the flux linkage maps and tests under load with related thermal measurements; the experimental findings are compared with the model results demonstrating an excellent match.**

***Index Terms*—AC machines, ferrite-assisted synchronous machines, lifting systems, synchronous reluctance machines.**

I. Introduction

In recent years, the Synchronous Reluctance (SyR) machine has drawn attention for its manufacturing simplicity and high efficiency. Indeed, the absence of Permanent Magnets (PMs) makes the SyR motors cost-competitive against the more performing PM synchronous machines (PMSMs) [1]. Besides the lower torque per volume, the SyR machine usually requires a larger inverter current, with respect to PMSMs, for the same torque and speed specifications, due to the lower power factor.

The recent peak of rare-earth materials cost (see the neodymium price in Fig. 1, from [2]) is pushing the industry to consider alternative solutions to PMSMs such as SyR machines and ferrite-assisted SyR (PM-SyR) machines. Notably, the ferrite price is quite stable although its main composite, the ferrite oxide, had experienced a 30% rise between 2021 and 2022 [3].

The present work is funded by ITG Tecnologie S.r.l, Rovereto, Italy and by the Power Electronics Innovation Center (PEIC) of Politecnico di Torino, Torino, Italy.

Dealing with electric machines for lifting purposes, the most challenging figures of merit are passenger comfort, allowable load, travel speed, landing precision and low energy consumption [4]. The traditional systems, based on DC motors and induction motors (IMs) [5] are progressively replaced by low-speed gearless PMSMs based on rare-earth PMs, thanks to their higher efficiency and compactness, associated with noise reduction and excellent control performance providing safety and comfort. In [6], a PM-SyR machine is compared with a rare-earth Surface-mounted PM (SPM) machine to drive an elevator system; the research demonstrated a cost reduction of 60% in favour of the ferrite. In [7], the feasibility of ferrite-assisted PM-SyR machines with a high number of poles was assessed, in replacement of NdFeB-based SPM machines. While, in [8] the authors describe the design and testing of a SyR machine for elevator traction, finalizing the research with a small-batch trial production.

This paper investigates SyR and PM-SyR machines for lifting applications. The paper aims at providing design guidelines corroborated by experimental validation and a comparison between these two types of machines. The target application is gearless lifting with the electric motor directly connected to the lifting system sheave [9], resulting in rotational speeds

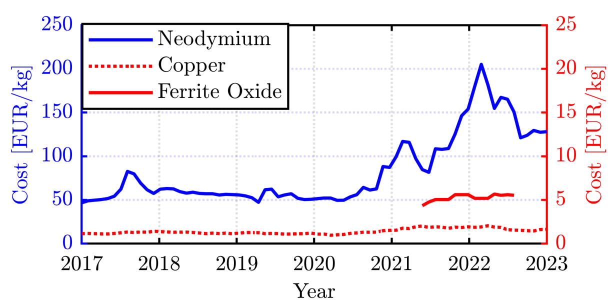

Fig. 1. Neodymium, ferrite oxide (main composite of ferrite) and copper price trends over the last 6 years according to [2] [3].

TABLE I
DESIGN REQUIREMENTS.

Nominal torque	T_N	1	[pu]
Peak torque	T_{max}	2.56	[pu]
Maximum speed	n_{max}	1	[pu]
Stator outer diameter	D	1	[pu]
Stack length	L	0.840	[pu]
Shaft diameter	d_s	0.280	[pu]
Airgap thickness	g	0.002	[pu]
Housing thickness	w_{hous}	0.034	[pu]
Max copper temperature	$\Theta_{Cu,max}$	140	[°C]

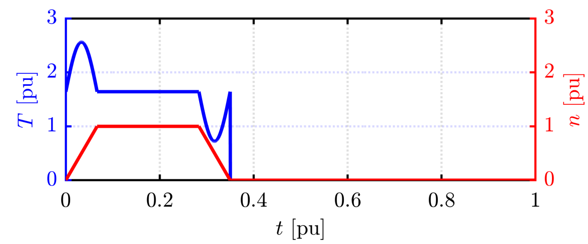

Fig. 2. Torque and speed envelope over one reference duty cycle.

in the order of few hundreds of rev/min or lower, and correspondingly high torque ratings. The first section proposes a parameterised approach for a quick preliminary design of the SyR [10] and PM-SyR [11] machines based on the dimensional, torque and speed requirements listed in Tab. I. The design requirements are common to the SyR and PM-SyR motor solutions. Note that having the same dimensions for the same torque and speed output, the SyR and PM-SyR machine design will necessarily have different inverter current ratings; this will shift part of the cost saving from the motor to the power converter side. The two machine types are analysed in terms of performance and production cost. Finally, the SyR machine prototype is manufactured and tested, and thermal experimental results are discussed.

The study is carried out with the open-source e-motor design framework SyR-e [12], developed by some of the authors and openly available to the public.

II. PRELIMINARY DESIGN PROCESS

The core of the design process is the (x, b) design plane [10], where key performance figures are displayed as a function of the geometric input parameters x and b:

$$x = \frac{D_r}{D} \qquad b = \frac{B_g}{B_{Fe,s}} \tag{1}$$

where D_r is the rotor diameter, D is the stator diameter, and B_g and $B_{Fe,s}$ are the airgap and back iron peak flux density values.

The design is carried out with reference to the specified lifting system duty cycle displayed in Fig. 2. From the average temperature standpoint, the periodic duty cycle is equivalent to a continuous torque equal to rms torque value T_N, defined as (2).

$$T_N = \sqrt{\frac{1}{t_c}\int_0^{t_c} (T(t))^2\, dt} = \ 1 \text{ pu} \tag{2}$$

Where t_c is the duty cycle period and t the variable time. Iron and PM loss effects are negligible, thanks to the low speed. Also, temperature undulation is negligible, due to the short duration of the cycle with respect to the thermal time constant of the non-ventilated machine. The T_N value obtained from the duty cycle is the base value for the per-unit normalization. Consequently, the peak torque of the cycle is 2.56 p.u., as in Fig. 2.

A. Design inputs

The magnetic design is carried out with reference to the target peak operating point; however, the thermal loading is chosen accordingly to the nominal point (i.e. continuous operation S1). Indeed, the operating point can be either fixed by the target current density or by the target thermal loading; its nominal value $k_{j,N}$ is defined as in (3).

$$k_{j,N} = \frac{\frac{3}{2} R_s i_N^2}{\pi D L} \tag{3}$$

Where i_N is the nominal (continuous) current, R_s is the stator resistance and L is the stack length. The use of thermal loading is suggested when the cooling specifications are rigid. Also, note that to compute the thermal loading in closed form with no need for simulations, this refers only to copper loss or standstill conditions. However, for low-speed motors such as the one under study, DC copper losses represent the majority of total losses, as later verified in section IV-A.

Considering copper insulation of class F, the starting $k_{j,N}$ is fixed to 5.5 kW/m^2 by using the simplified 2-dimensional thermal network presented in [13]. Note that the adopted thermal circuit is oversimplified and that later thermal tests reported a lower value of $k_{j,N}$, equal to 4 kW/m^2; further comments on thermal loading are provided in section IV-E.

The peak value $k_{j,pk}$ is found from $k_{j,N}$ and the torque overload factor, assuming a proportional relationship between torque and current (4).

$$k_{j,pk} = \left(\frac{i_{max}}{i_n}\right)^2 k_{j,N} \approx \left(\frac{T_{max}}{T_N}\right)^2 k_{j,N} = 36 \text{ kW/m}^2 \tag{4}$$

Note that this approach is conservative from a thermal point of view: indeed, once the peak torque corresponds to the target $k_{j,pk}$, the nominal torque will be obtained with $k_j < k_{j,N}$ because of iron saturation.

At this stage, to quickly evaluate the optimal numbers of pole pairs p and slots per pole per phase q, three combinations have been investigated using the (x, b) design plane: p3q2 (namely, 3 pole pairs and 2 slots per pole per phase), p4q2 and p3q3. For each option, a design plane with $k_{j,pk} = 36$ kW/m^2 is computed and the key performance contours are plotted.

B. Design planes and selected SyR machines

The design planes are the result of analytical equations combined with the fast finite element analysis (FEA) correction

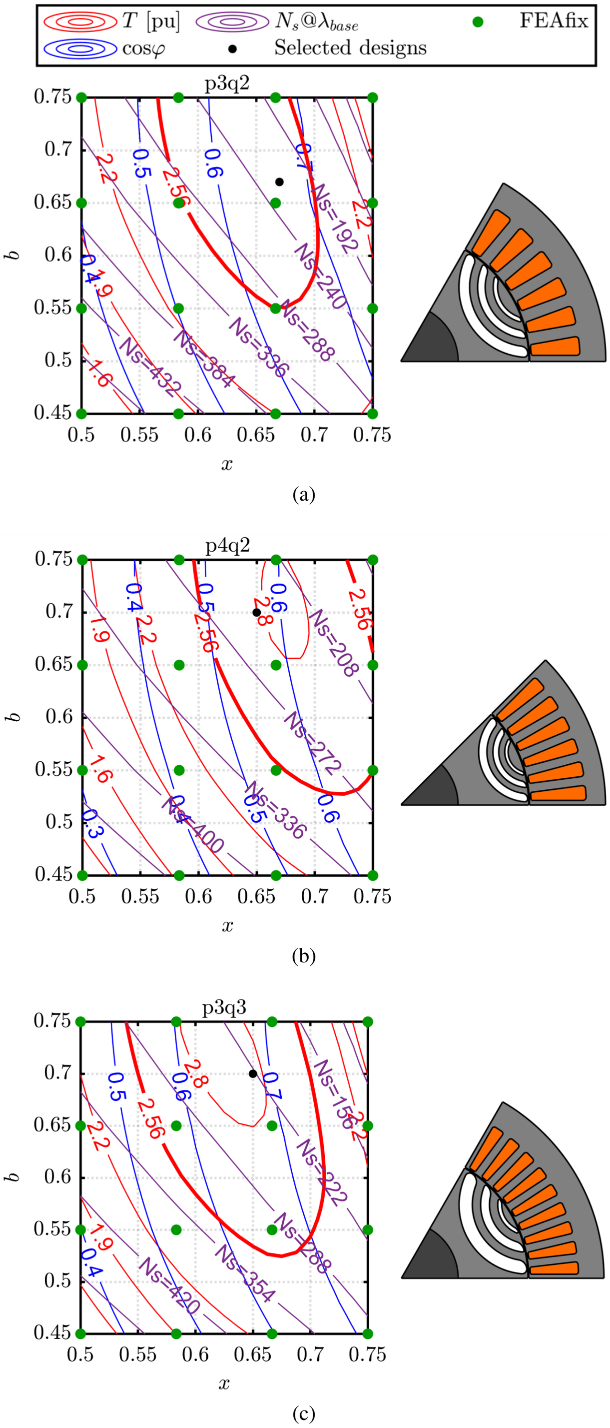

Fig. 3. Design planes with (a) p=3 and q=2, (b) p=4 and q=2 (c) p=3 and q=3, where p indicates the number of pole pair and q the number of slots per pole per phase.

FEAfix method, as discussed in [11]. The FEAfix approach uses a 4x4 grid of FEA simulations on the design plane to calibrate the design equations; this achieves a high level of accuracy maintaining an agile computational time: about 20 minutes using a PC with an Intel Xeon E5-2690 v4, 32GB RAM and 14 cores. The FEAfix simulated designs are marked with green dots in Fig. 3. Each of the 16 FEAfix designs is evaluated at the correct Maximum Torque per Ampere (MTPA) phase angle conditions, obtained through iteration.

The planes report the torque contours, as well as the power factor and N_s contours, defined later, all at MTPA conditions. The highlighted peak torque contours (2.56 p.u.) enclose the area of feasible designs. Power factor-wise, a larger power factor reduces the peak current requirement, provided that the peak torque specification is met. The N_s@λ_{base} contours correspond to the designs that meet the specified base speed n_{base} at the maximum inverter voltage and N_s turns.

Note that meeting the target n_{base} requirement corresponds to avoiding the need of flux-weakening operation, which is also a design goal. The plane region above each N_s contour meets the base speed requirement. Only feasible numbers of turns are plotted.

For each plane, a motor is selected, fulfilling the torque and base speed requirements, and with maximized power factor, given the feasible number of turns. The cross-sections of the selected designs are shown in Fig. 3, with their position in the corresponding design plane marked with a black dot. Ansys Motor-CAD [14] is used to compute the peak copper temperature of each SyR motor over the reference duty cycle (Tab. II) repeated several times. The output figures of the three candidates are summarized on the left side of Tab. II; after thermal comparison, the p4q2 design is indicated as the final SyR machine design for having the lowest copper temperature over the reference duty cycle.

C. PM-SyR motor

A first PM-SyR design p4q2-v1, displayed in Fig. 4a, was obtained using the stator of the p4q2 SyR machine, for ease of comparison and for economy of scale manufacturing wise. On the rotor, segmented barriers are used for inserting straight PM pieces, maintaining the positions of the barrier ends at the airgap and the barrier thicknesses the same as the p4q2 SyR machine design. The rotor design is further refined for reducing the PM part count as shown in Fig. 4b, where the second PM-SyR design p4q2-v2 has barriers of equal thickness and the one on top of the pole I-shaped. For sake of clarity, in Fig. 4 the different sizes of dimensions are numbered.

The steady-state demagnetization current limit is evaluated through FEA simulations. An iterative procedure is implemented to identify the current that demagnetizes 1% of the

TABLE II
MOTORS COMPARISON.

	SyR			PM-SyR	
	p3q3	p4q2	p3q2	p4q2-v1	p4q2-v2
Number of turns	297	272	288	272	272
Peak current [pu]	1.93	2.09	2.03	1.78	1.83
Demag current [pu]	-	-	-	2.27	2.13
Cycle avg loss [pu]	0.98	1	1.05	0.73	0.8
Cu pk temperature [pu]	1.06	1	1.01	0.76	0.83
PM mass [kg]	0	0	0	4	3.7
Set of PM dimensions	0	0	0	6	3

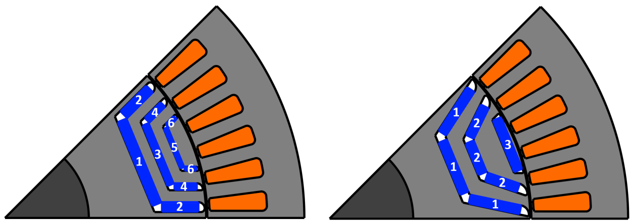

(a) (b)

Fig. 4. The PM-SyR motor (a) before and (b) after PM cost optimization, respectively p4q2-v1 and p4q2-v1. The ferrite magnets are highlighted in blue.

PM volume at the rated PM temperature. From the results reported in Tab. II, it can be noticed that PMs are always safe against demagnetization during operation; the p4q2-v2 motor is slightly penalized compared to the p4q2-v1, but it is still safe against demagnetization.

III. Cost comparison

Comparing different solutions in terms of cost can be a challenging task. For instance, in [15], the focus is on minimizing material costs and losses to optimize production and operating costs, but the study does not provide a detailed cost breakdown. On the other hand, [16] performs a more specific comparison of rare-earth magnet materials in terms of costs and benefits, while [17] presents a comprehensive cost breakdown that highlights the cost-saving potential of using ferrite instead of rare-earth magnets with fixed stack dimensions.

In this section, a cost analysis is conducted for two designed motors based on the material quotes of early 2022, and the results are presented in Tab.,III. The analysis shows that iron contributes the most to the motor's cost, with stator and rotor iron accounting for 24% and 22%, respectively. Since the two motors have the same stack dimensions and winding configuration, the difference in total cost is mainly attributed to the magnets and their mounting, which represent 9% and 2% of the total cost of the SyR machine, respectively. Overall, the PM-SyR machine exhibits an 11% cost increase compared to the SyR machine due to the presence of magnets.

However, it is important to note that at fixed performance and stack dimensions, the SyR motor requires a larger peak current, which results in the need for a power converter with a current rating increased by 14%. Additionally, the SyR motor has a higher thermal loading and requires a fan to fully cover the reference duty cycle, and the fan adds to the cost, complication and efficiency, although not substantially. Taking into account the bigger converter and fan, it is pretty sure that the cost balance would shift from the SyR to the PM-SyR machine solution.

TABLE III
Cost breakdown

	SyR p4q2	PM-SyR p4q2-v2	
Stator iron	0.24	0.24	[pu]
Copper	0.18	0.18	[pu]
Winding labour	0.13	0.13	[pu]
Rotor iron	0.22	0.22	[pu]
Ferrite	0	0.09	[pu]
Shaft	0.15	0.15	[pu]
Labour	0.09	0.11	[pu]
Total Cost	1	1.11	[pu]

IV. SyR Motor Prototype and Tests

This section reports the additional design studies of the p4q2 SyR machine prototype and the experimental results.

A. AC loss

Dealing with loss analysis, AC copper and iron loss can be neglected because of the low fundamental frequency (always lower than 10 Hz). Here, this assumption is verified by FEA simulations: with reference to the p4q2 SyR motor, the loss breakdown is reported in Tab. IV. It is evident that the high DC resistance value and the low operating frequency make the AC loss contributions insignificant. The loss analysis is conducted with the methodologies presented in [18].

Furthermore, the inverter modulation impact on the loss is not included due to high winding inductance and thus very low current ripple [19].

TABLE IV
SyR p4q2 Loss breakdown for the duty cycle point at maximum speed

DC Copper	AC copper	Iron
1 pu	$5 \cdot 10^{-5}$ pu	0.013 pu

B. Skew Angle

The skew angle θ_{skew} in mechanical degrees is defined after the target torque ripple harmonic order h to be minimized as in (5).

$$\theta_{skew} = \frac{360}{p \cdot h} = 7.5^\circ \tag{5}$$

In this case, $h = 12, p = 4$ and thus $\theta_{skew} = 7.5^\circ$. The flux and torque maps are recalculated after skewing using the multi-slice approach [20] and the $dq\theta$ maps [21], where torque and flux linkage maps are a function of the rotor position, besides the dq currents. Doing so, the $dq\theta$ flux maps are off-line

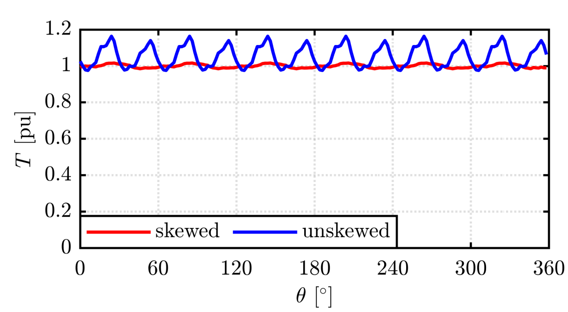

Fig. 5. Torque waveform for unskewed (blue) and skewed (red) motors at nominal current and MTPA.

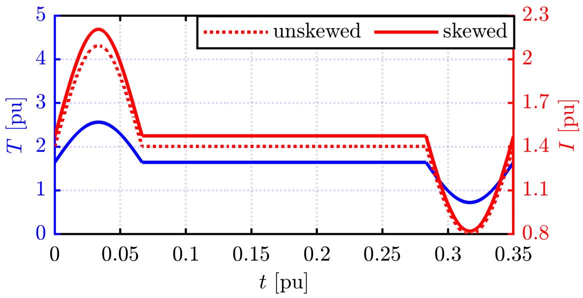

Fig. 6. Requested current over a duty cycle for unskewed and skewed motors.

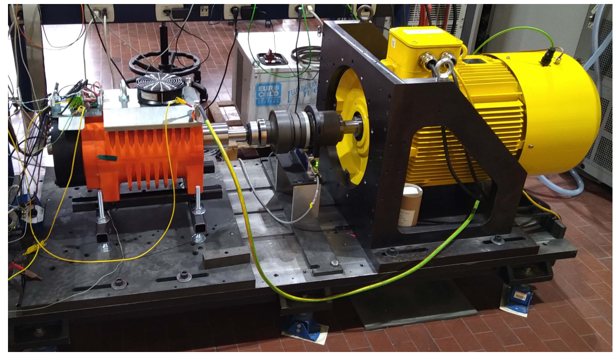

Fig. 8. Prototype of the p4q2 SyR machine (left) mounted on the test rig.

manipulated within a few minutes by shifting, interpolating and summing properly the FEA waveforms stored in the maps, without running any dedicated FEA simulation.

The maximum torque ripple requirement of 5% peak-to-peak at maximum torque is fulfilled for the SyR machine with the said angle and 5 step-skewed rotor segments. Fig. 5 compares the non-skewed and skewed torque waveforms at nominal current and MTPA conditions, highlighting the torque ripple elimination. Conversely, the skewed motor needs a higher current to match the average torque of the straight version. Fig. 6 compares the current amplitude profile of the two machines (skewed and not) throughout the reference duty cycle. The current difference is evident and results in a loss increase of 10% on average over a cycle.

C. Test Campaign and Experimental setup

The p4q2 SyR motor was manufactured and tested to validate the magnetic and thermal models, as visible in Fig. 8. The fan visible on the top side is used to comparatively assess the possible benefits of ventilation. The experimental validation consists of:

- flux maps identification at constant speed [22];
- heating test at constant current;
- heating test at the reference duty cycle, with the fan initially on and then turned off.

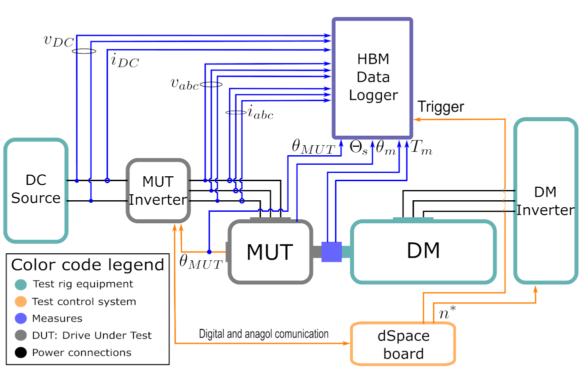

Fig. 7. Schematic of the test rig setup for the magnetic and thermal measurements.

The experimental setup is illustrated in Fig. 7 and consists of the Motor Under Test (MUT) and a Driving Machine (DM). The former is supplied by a custom inverter and current controlled using a dSPACE fast prototyping board, while the latter is speed controlled from a custom drive. Dealing with the measurement system, it is based on the HBK Gen7ta data recorder. Electrical, mechanical and thermal quantities are measured and stored for triggered time frames, with the trigger managed by the dSPACE control board. The measured quantities are the line voltages (direct measure), phase currents (200A Ultrastab LEM sensors), torque and speed (measured using a 100Nm HBM T40B torque meter), end-winding (copper 1) and in-slot (copper 2), housing and ambient temperatures.

D. Flux map identification

Flux maps are measured at 0.3 p.u. constant speed with the method described in [22]: for each point of a square i_{dq} grid, three sweeps are recorded, two in motor operation and one in symmetric generator operation, obtained by changing the sign of the q axis current. The three sweeps are used to cancel the resistance voltage. The line voltage and phase currents are transformed in dq coordinates and properly averaged to obtain the dq flux linkages function of the dq currents. In Fig. 9, the flux linkage contours are displayed on the dq current plane and compared to the corresponding FEA curves. The experimental measurements (blue solid lines) and the FEA simulation results (red dotted lines) are well matched. The deviations of the d flux linkage for low i_q and large i_d values are outside the MTPA trajectory, so their effect is minor. A possible source of inaccuracy is the B-H curve of the laminated steel reporting typical values and not accounting for degradation caused by laser cut. The torque contours and MTPA trajectories are reported and compared in Fig. 10, also showing a reasonably good match between FEA and measurements.

The torque function of the current amplitude under MTPA condition is reported in Fig. 11, again comparing measurements and FEA estimates. The match between the two curved is almost perfect. The torque error, expressed in percent of the measured torque, is reported in green, and it is lower than 4% for low load values, and 2% at nominal torque. Altogether, the FEA model is well validated by the experiments, advocating

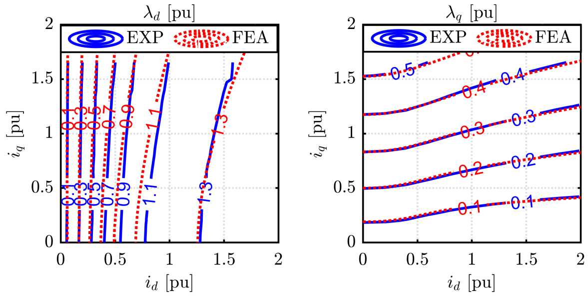

(a) (b)

Fig. 9. Comparison between experimental measurements and FEA model: (a) d and (b) q flux linkage as a function of the dq current.

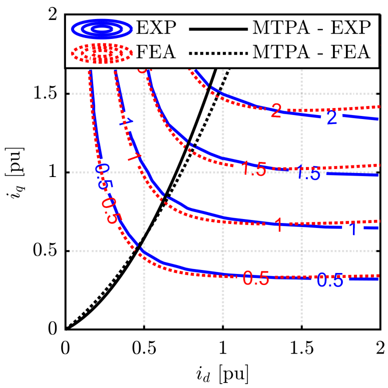

Fig. 10. Comparison between experimental measurements and FEA model: electromagnetic torque as a function of the dq current and MTPA trajectories.

for a good quality of both the design and manufacturing processes.

E. Heating tests

Two heating tests are executed, one at constant current and one with periodic intermittent service, with a reference duty cycle. Four temperatures are logged using thermocouples; they are ambient temperature (Θ_{amb}), housing temperature ($\Theta_{housing}$), end-winding temperature ($\Theta_{Cu,1}$) and inside slot temperature ($\Theta_{Cu,2}$).

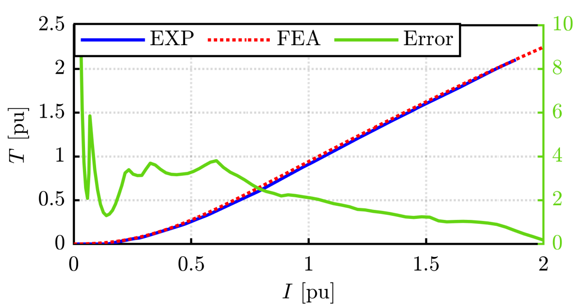

Fig. 11. Comparison between experimental measurements and FEA model: current vs torque in MTPA condition.

First, the constant nominal current is imposed for 180 minutes with the fan initially OFF. The recorded temperatures are reported in Fig. 12a. After 65 minutes the fan is switched ON to keep the winding temperature below the precautionary level of 120°. This test demonstrates that the SyR motor can sustain the target continuous torque for three hours with without exceeding the thermal limit (120°C at 20°C ambient is close to the class F limit of 145°C at 40°C ambient), provided that the motor is ventilated. Furthermore, this test is also useful for thermal model calibration.

Dealing with the periodic intermittent duty-cycle service test, this is started with the fan activated, as reported in Fig. 12b. After 3 hours of work, representing the target working time, the fan is turned off and the test is continued. The maximum winding temperature under ventilation is around 80°C, demonstrating that the adopted duty cycle is very well sustained by the SyR motor with ventilation, and this is also true with hotter ambient temperatures. Without ventilation, the maximum temperature is around 115°C after another 90 minutes.

It is worth noting that, from design inputs, an infinite sequence of duty cycles should be sustained without ventilation. The tests highlighted that the thermal model in the design process was optimistic and that ventilation is needed to sustain the target operating cycle fully. Therefore, the thermal model of the motor must be calibrated after the test, because of some assumptions that were not possible to fulfil during the industrial manufacturing of the motor. This data will be useful for the further design review of the SyR motor, before its launch on the market. A second point that must be addressed

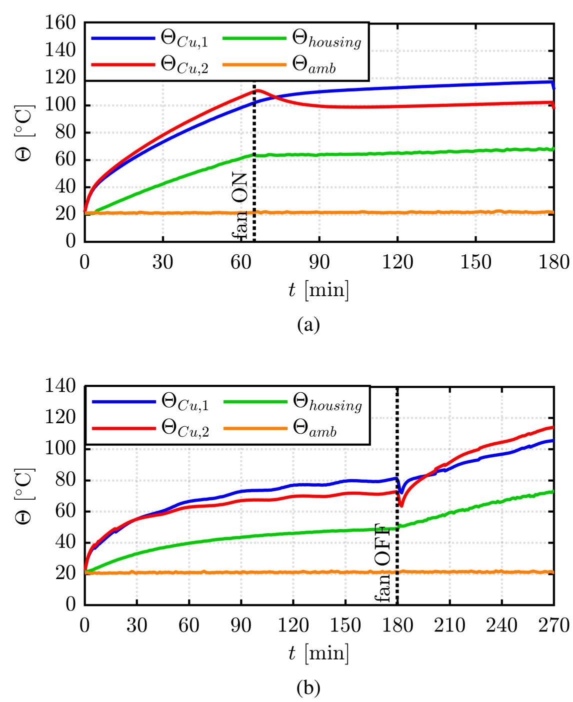

(a)

(b)

Fig. 12. (a) Temperature measurements at a constant current of 1pu with the fan OFF up to 60 minutes and then ON; (b) temperature measurements over repeated duty cycles with the fan ON up to 180 minutes and then OFF.

is the difference between the maximum temperatures after 3 hours with constant torque and intermittent periodic duty-cycle torque. This working point should be thermally equivalent to assumption, but the tests demonstrate that there is a small difference. This could be caused by a non-perfect duty-cycle control (torque variations are limited for mechanical problems on the test rig). A second cause of discrepancy could be the assumption to have a proportional relationship between torque and current in (4). This is not exactly true, but the actual relationship between torque and current along the MTPA is known after the computation of the magnetic model of the motor, and not in the design stage.

V. Conclusion

This paper presents the design process and comparison between SyR and ferrite-assisted PM-SyR motors for lifting applications. The design process is based on the reference duty cycle typical of the application and uses the (x, b) design plane. Various solutions are compared in terms of performance and cost. The PM-SyR motor is optimized in terms of PM part count to reduce costs; however, the SyR solution still proves to be more cost-effective. To validate the design, the final SyR motor is built and tested, demonstrating good agreement between FEA simulated outputs and measured performance figures. The open-source environment SyR-e is adopted in the design process, and this experimental validation is a further step in the validation of the software. The heating tests conducted with and with ventilation highlight the thermal issues of this motor and provide data for the thermal model calibration. This study represents the first stage in designing a family of SyR motors for lifting applications, and the open-source software SyR-e is freely available for the academic and industrial community.

Acknowledgment

The research is the outcome of the joint work between ITG Tecnologie S.r.l. and Power Electronics Innovation Center (PEIC) of Politecnico di Torino.

References

[1] Y. Avsar, A. Fenercioglu, and M. Soyaslan, "Design optimization of PM synchronous motor used in belt drive elevator systems," in *2021 IEEE 4th International Conference on Computing, Power and Communication Technologies (GUCON)*, pp. 1–5.

[2] TRADING ECONOMICS | 20 million INDICATORS FROM 196 COUNTRIES. [Online]. Available: https://tradingeconomics.com/

[3] P. Fears. Ferrite magnet price trends. [Online]. Available: https://www.bunting-berkhamsted.com/ferrite-magnet-price-concerns/

[4] J. Wang, F. Tan, and R. Jin, "Research on low-speed gearless permanent magnet synchronous motor for elevator drive," in *2005 International Conference on Electrical Machines and Systems*, pp. 454–459 Vol. 1.

[5] O. V. Kruglikov, "Low-speed induction motors for directly driven elevator machines," vol. 86, pp. 118–124.

[6] H. Yetiş, E. Meşe, and M. Biyikli, "Design and comparison of ferrite based IPM and NdFeB based SPM synchronous motors for gearless elevator systems," in *2018 XIII International Conference on Electrical Machines (ICEM)*, pp. 635–641, ISSN: 2381-4802.

[7] B. Boazzo, A. Vagati, G. Pellegrino, E. Armando, and P. Guglielmi, "Multipolar ferrite-assisted synchronous reluctance machines: A general design approach," vol. 62, no. 2, pp. 832–845.

[8] J.-C. Li, M. Xin, Z.-N. Fan, and R. Liu, "Design and experimental evaluation of a 12 kW large synchronous reluctance motor and control system for elevator traction," vol. 8, pp. 34 256–34 264.

[9] K. Al-Kodmany, "Tall buildings and elevators: A review of recent technological advances," vol. 5, no. 3, pp. 1070–1104.

[10] S. Ferrari and G. Pellegrino, "FEAfix: FEA refinement of design equations for synchronous reluctance machines," vol. 56, pp. 256–266.

[11] P. Ragazzo, G. Dilevrano, S. Ferrari, and G. Pellegrino, "Design of IPM synchronous machines using fast-FEA corrected design equations," in *2022 International Conference on Electrical Machines (ICEM)*.

[12] F. Cupertino and G. Pellegrino. SyR-e. [Online]. Available: https://github.com/SyR-e

[13] M. Gamba, G. Pellegrino, E. Armando, and S. Ferrari, "Synchronous reluctance motor with concentrated windings for ie4 efficiency," in *2017 IEEE Energy Conversion Congress and Exposition (ECCE)*, 2017, pp. 3905–3912.

[14] Ansys motor-CAD. [Online]. Available: https://www.ansys.com/en-gb/products/electronics/ansys-motor-cad

[15] P. Zhang, D. M. Ionel, and N. A. O. Demerdash, "Saliency ratio and power factor of IPM motors with distributed windings optimally designed for high efficiency and low-cost applications," vol. 52, no. 6, pp. 4730–4739.

[16] Z. Zarkov, V. Lazarov, T. Stoyanov, and L. Stoyanov, "Influence of magnet dimensions on torque components and cost of synchronous machine with interior magnets," in *2021 17th Conference on Electrical Machines, Drives and Power Systems (ELMA)*, pp. 1–6.

[17] Z. Zhang, "Design and experimental verification of low cost ferrite PM-assisted synchronous reluctance motor," in *2020 IEEE Transportation Electrification Conference & Expo (ITEC)*, pp. 327–334.

[18] S. Ferrari, P. Ragazzo, G. Dilevrano, and G. Pellegrino, "Flux and loss map based evaluation of the efficiency map of synchronous machines," pp. 1–10.

[19] A. Hava, R. Kerkman, and T. Lipo, "Simple analytical and graphical methods for carrier-based pwm-vsi drives," *IEEE Transactions on Power Electronics*, vol. 14, no. 1, pp. 49–61, 1999.

[20] R. Islam, I. Husain, A. Fardoun, and K. McLaughlin, "Permanent-magnet synchronous motor magnet designs with skewing for torque ripple and cogging torque reduction," *IEEE Transactions on Industry Applications*, vol. 45, no. 1, pp. 152–160, 2009.

[21] S. Ferrari, G. Dilevrano, P. Ragazzo, and G. Pellegrino, "The dq-theta flux map model of synchronous machines," in *2021 IEEE Energy Conversion Congress and Exposition (ECCE)*, pp. 3716–3723, ISSN: 2329-3748.

[22] E. Armando, R. I. Bojoi, P. Guglielmi, G. Pellegrino, and M. Pastorelli, "Experimental identification of the magnetic model of synchronous machines," vol. 49, no. 5, pp. 2116–2125.